JOURNAL OF MATERIALS SCIENCE 19 (1984) 3524–3545

Changing the surface mechanical properties of silicon and α-Al_2O_3 by ion implantation

P. J. BURNETT, T. F. PAGE
Department of Metallurgy and Materials Science, University of Cambridge,
Pembroke Street, Cambridge, CB2 3QZ, UK

Microhardness indentation testing has been used as a means of introducing controlled localized deformation and fracture in both ion-implanted and unimplanted {1 1 1} silicon and $\{10\bar{1}2\}$ sapphire single crystal surfaces. The microstructural alterations due to implantation with N_2^+ and Al^+ into silicon and Y^+ into sapphire have been characterized using channelled Rutherford backscattering, transmission electron microscopy and electron channelling in the scanning electron microscope. It was found that sapphire only became amorphous at doses $\gtrsim 3 \times 10^{16}$ $Y^+ cm^{-2}$ which corresponds to a total energy deposition of $\sim 3 \times 10^{23}$ keV cm^{-3} (~ 44 kJ mm^{-3}). The low-load microhardness (< 50 gf) was found to be sensitive to the thickness of the amorphous layer produced by implantation into both silicon and sapphire. Compared with the parent crystal, this layer was found both to be softer and to behave in a relatively plastic manner with considerable plastic pile-up occurring around indentations in the higher dose specimens. The indentation fracture behaviour was found to be dominated by the presence of implantation-induced compressive stresses. The resulting effects were: (a) a decrease in the size of the radial crack traces (hence K_{IC} is apparently increased when evaluated using indentation fracture mechanics), (b) a decrease in the frequency of occurrence of lateral break-out in silicon and subsurface lateral cracking in sapphire, (c) initiation of lateral cracks further below the surface in both silicon and sapphire. Thus in general, it is concluded that hardness and surface plasticity are associated with softer amorphous layers whilst indentation fracture modifications are principally stress related.

1. Introduction

Recently there has been considerable interest in ion implantation as a surface treatment process in several fields outside the semiconductor industry; notably for altering corrosion and tribological behaviour, e.g. [1, 2]. The work presented here is part of a programme investigating how the surface contact response and wear behaviour of hard ceramic materials may be influenced by ion implantation.

A previous study in this programme demonstrated that the implantation of both silicon and silicon carbide with N_2^+ ions above a "critical dose" of $\sim 4 \times 10^{17}$ ions cm^{-2} resulted in a significant softening of the surface coupled with a suppression of the lateral crack breakout which results in removal of material during both indentation and abrasive wear of brittle materials [3]. Further, a previous paper by us [4] has correlated the surface softening specifically with the formation, size and position of a radiation-induced layer of amorphized material and has shown that the "critical dose" corresponds to that at which a large change in amorphous layer thickness occurs. In addition, a model to describe quantitatively the development, extent and position of this layer has been presented [4].

Using single-crystal silicon and single-crystal

0022–2461/84 \$03.00 + .12

sapphire as model covalently bonded and ionically bonded brittle materials respectively, this paper reports the extensive effects of ion implantation, as a function of dose, upon the surface and near-surface deformation and fracture induced by indentation techniques. Also, the amorphization model has been used to estimate the expected damage patterns (for instance whether sub-surface or surface amorphous layers are produced at a given dose) and thus extend the study of the effects of progressive amorphization to sapphire. Further, the effects of implantation-induced stresses and their influence upon indentation fracture are considered.

In order to understand more fully the changes that occur in the fracture/plasticity behaviour of these materials, and to complement the damage calculations, the levels and distribution of radiation damage have been monitored by a range of microstructural techniques. These included (a) channelled Rutherford backscattering (RBS) techniques, (b) electron channelling in the scanning electron microscope (SEM) and (c) electron diffraction in the transmission electron microscopy (TEM). From the results of these studies the critical energy deposition needed to amorphize sapphire has been estimated.

2. Specimen preparation

Single crystal semiconductor grade silicon wafers (courtesy of Texas Instruments) of ~ 3° off $-\langle 111\rangle$ sheet normal and bulk impurity content of either 9.4×10^{13} Sb atoms cm^{-3} or 5.4×10^{14} Sb atoms cm^{-3} were implanted with N_2^+ and Al^+ ions respectively. Table I shows the doses and energies used which, using the quantitative model described by Burnett and Page [4], were chosen to give a range of amorphous layer sizes from ~ 0.4 to 0.8 μm. Sapphire wafers of $\{10\bar{1}2\}$ section (courtesy of GEC (Wembley)) were implanted with 300 keV Y^+ to the doses in Table I. Yttrium was chosen as the ion species for implantation into sapphire partly because it is isovalent with aluminium and partly because of the possibility of forming either yttria or yttrium–aluminium–garnet precipitates on subsequent annealing (work in progress). Both silicon and sapphire wafers were supplied with one side pre-polished to a mirror finish and no further surface treatments besides degreasing were performed prior to implantation.

The Al^+ and Y^+ implantations were performed in the Cockcroft-Walton 500 keV implantation facility at AERE Harwell. The specimens were cleaved along the traces of the $\{1\bar{1}0\}$ planes for silicon and the $(1\bar{1}02)$ and $(0\bar{1}12)$ planes for sapphire to give a maximum caliper diameter of ~ 25 mm. For both ion species, the singly-charged ion was extracted and then scanned across the target. The dose rate was typically 3 to 4 μA cm^{-2} leading to a rise in specimen temperature of ~ 250° C during implantation. The dose was calculated from the counts on the target. However, for the insulating sapphire this proved unreliable and the actual dose was measured using non-aligned Rutherford backscattering (RBS) of 2 MeV He^+ ions in the intense bunched ion source (IBIS) 3 MeV Van der Graff generator at AERE Harwell. A solid-state detector at an angle of 160° to the incident beam was employed, and the resulting spectrum analysed using the "Caliph" RBS operating system [5] to yield the actual dose of yttrium in each specimen.

The nitrogen implantations were performed in the Harwell "PIMENTO" prototype commercial implantation machine [2]. A non-mass-analysed beam of nominally N_2^+ at 90 keV is produced, the actual composition of the beam being ~ 75% N_2^+ at 90 keV + 25% N^+ at 90 keV. The N_2^+ ions are assumed to split into $2 \times N$ at 45 keV on contact with the surface and hence the actual dose is $7/4 \times$ the "stated dose" of N_2^+. Again the average dose rate was a few μA cm^{-2} giving rise to a temperature change of ~ 250° C. Since the specimen area is large in this machine, whole wafers were implanted.

3. Radiation damage and the amorphous transformation

Ion bombardment of any form will introduce defects into a crystalline solid. In ion implantation, much of the energy of the ion is given up in elastic collisions (the remainder being dissipated by electronic processes) which result in the formation of "Frenkel pairs" whereby an atom is displaced from its structure site to form a vacancy-interstitial pair (displacement damage). At high ion doses, the cumulative effect of the displacement damage due to implantation can be to completely randomize (amorphize) regions of the crystal where a critical level of displacement damage (hence the level of energy deposition) has been exceeded [4, 6]. Beneath the surface, the damage profile is approximately Gaussian and this results

TABLE I Ion energies, doses, implant peak width and amorphous layer thicknesses

Specimen		Dose (ions cm^{-2})	Energy (keV)	Implant peak width (μm)‡	Amorphous layer thickness (μm)		Additional surface state information	
					Predicted	Experimental (RBS)	SEM/ECP	TEM/SADP
Silicon:	SU101	0	–	–	–	–	–	–
	SI101	1.0×10^{17} N_2^+*	90	–	0.43	0.46(a)	(d)	(a)
	SI102	2.0×10^{17} N_2^+*	90	–	0.45	0.47(a)	(a)	
	SI104	4.0×10^{17} N_2^+*	90	–	0.46	0.50(a)	(a)	
	SI106	6.0×10^{17} N_2^+*	90	–	0.467	0.72(a)	(a)	
	SI108	8.0×10^{17} N_2^+*	90	–	0.47	0.73(a)	(a)	
	SI121	5.0×10^{17} Al^+	300	–	0.82	~ 0.8–0.9† (a)	(a)	
Sapphire:	AU1	0	–	–	–	–	–	–
	AY1	0.13×10^{17} Y^+	300	–	0.0	0.0	(d)	(d)
	AY2	0.28×10^{17} Y^+	300	0.165	0.0	0.0	(d)	(d)
	AY3	0.99×10^{17} Y^+	300	0.170	0.118	~ 0.14(s)	(a)	
	AY4	1.12×10^{17} Y^+	300	0.180	0.125	~ 0.15(s)	(a)	
	AY5	3.81×10^{17} Y^+	300	0.23	0.158	–	(a)	
	AY6	5.80×10^{17} Y^+	300	0.26	0.165	0.23(a)	(a)	(a)

*Implantation carried out in "Pimento" machine. See Section 2 for beam composition.

†The Al peak and damage peaks are superimposed on this spectrum thus making accurate determination of the damage and concentration peak widths difficult.

‡Determinations of the N_2^+ implant peak width were not undertaken due to difficulties with low count rates from the light implant species and the superposition of the implant peak on the background.

(a) = amorphous surface, (d) = damaged crystalline surface, (s) = sub-surface amorphous zone.

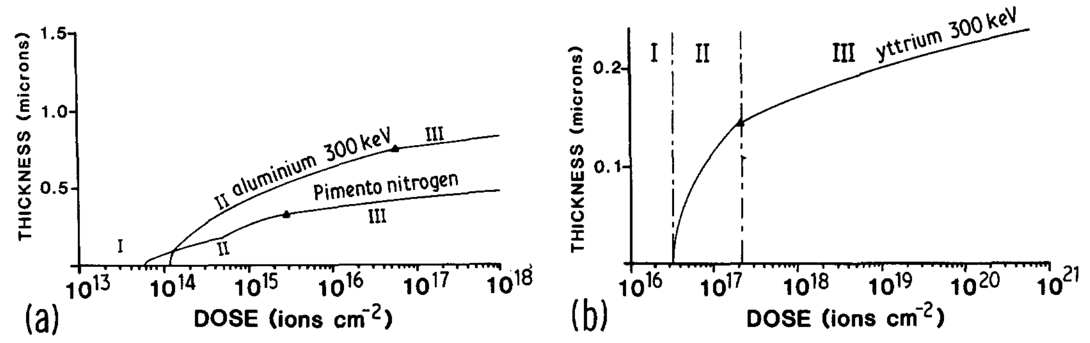

Figure 1 The predicted variation in size and position of the amorphous layer produced by ion implantation (a) into silicon with N_2^+ at 90 keV and Al^+ at 300 keV, and (b) into sapphire with Y^+ at 300 keV. Region I corresponds to the doses prior to amorphization, i.e. a crystalline but damaged surface, Region II corresponds to the formation of a sub-surface amorphous zone, whilst, in Region III, the layer extends inwards from the surface. The amorphization criteria used are 0.1 DPA for silicon (from [6]) and 2.8×10^{23} keV cm^{-3} for sapphire (as derived in the Appendix). In (a), note the kink in the "Pimento" nitrogen curve when the smaller 90 keV N^+ component of the beam becomes important.

in a sub-surface amorphous zone initially being formed as the dose (and hence displacement level) increases. With further increases in dose, this amorphous zone gradually thickens and eventually becomes a surface amorphous layer. In earlier work by the authors, a simple quantitative approach has been proposed to predict the position and extent of this amorphous layer [4]. Using this model together with the critical energies for amorphization of silicon [6] and sapphire (see the Appendix), the predicted variations of amorphous layer thickness with dose for the ion/energy/substrate combinations used here (see Table I) have been computed and are presented in Fig. 1.

An aligned RBS technique was adopted as a means of quantifying the extent of the displacement damage caused by ion implantation. Using the IBIS generator as previously described, the specimens were aligned so that the incident beam was along a suitable low-index crystallographic direction and hence in a channelling condition. In this configuration, the damaged regions of the specimen give rise to a greater amount of scattering than the undamaged crystal, resulting in a peak on the scattered ion energy spectra. The ⟨1 1 1⟩ direction close to the silicon surface normal and both the ⟨0 0 0 1⟩ axial and {0 0 0 1} planar channelling directions in sapphire (at 58° and 32° to the surface normal) were utilized. Fig. 2 shows

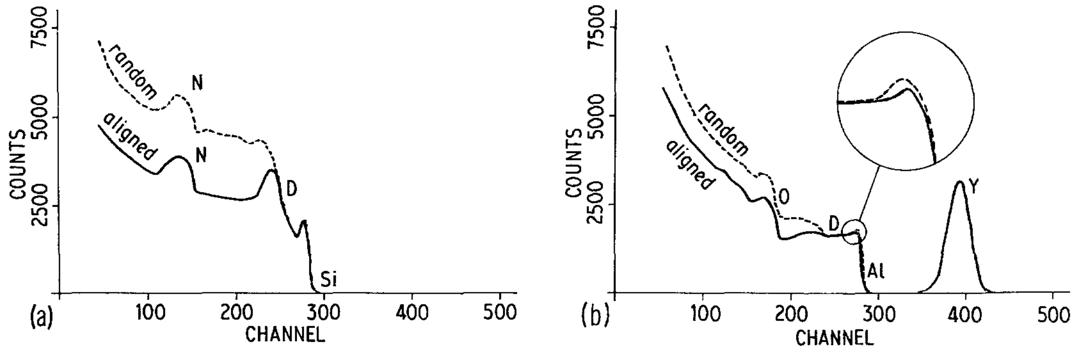

Figure 2 Random and aligned (channelled) RBS spectra: (a) SI108 ($8 \times 10^{17} N_2^+ cm^{-2}$) showing the implant peak (N), the silicon scattering edge (Si) and the damage peak (D), the latter being present in the aligned spectrum only; (b) AY3 ($0.99 \times 10^{17} Y^+ cm^{-2}$) showing the implant peak (Y), the aluminium and oxygen scattering edges (Al and O) and the damage "peak" (D). It might be expected that the "damage" regions of the "random" and "aligned" spectra from the amorphous layer would coincide. While this is virtually so for the Al_2O_3 samples (to the left of the Al edge), there is some divergence for the silicon sample. Also note the slightly reduced amount of scattering from the aligned Al_2O_3 spectrum near the surface (i.e. close to the Al edge) indicating that some channelling may still be occurring in the highly damaged surface layer (see Section 6.2).

typical spectra for a N_2^+ implanted silicon specimen and for a Y^+ implanted sapphire specimen.

Although the shapes of these two curves are superficially different, it can be seen that the spectra both show "peaks" due to amorphization of the crystal superimposed upon a channelled background. The spectra also show peaks due to the presence of the implanted species. The majority of the specimens were studied using this technique and the size of the amorphous layer determined (see [4] for details). The results of the RBS analyses are given in Table I together with those predicted from the range and damage parameters using the approach of Burnett and Page [4]. Also included in Table I are the dopant peak widths for the Y^+ implanted Al_2O_3 specimens and it may be seen that these are greater than the extent of the amorphous layer. Since the concentration profile is usually assumed to be Gaussian with a broader peak at a greater depth than the damage profile [7], this is as expected.

Microscopically, the extent of the damage introduced by ion implantation was studied by two methods: (a) electron channelling patterns obtained in the SEM, and (b) electron diffraction patterns obtained in the TEM. Since electron channelling is sensitive to the perfection of the crystal structure to a depth of ~ 100 nm, damage introduced by ion implantation will cause the channelling pattern to degrade [8, 9]. Fig. 3 shows wide area channelling patterns (WACP) obtained using a Camscan 4 scanning electron microscope operating at 30 kV with the scanned region spanning the implanted/unimplanted border. For specimens SI21, AY3 and AY6 it can be seen that there is no channelling pattern in the implanted region. This implies that these surfaces are either amorphous or highly damaged and these cases cannot be distinguished further by this technique alone (see Section 6.2). However, the channelling pattern obtained from specimen AY2 does show channelling in the implanted region although the pattern is degraded indicating that the crystal is imperfect. The WACP results are summarized in Table I and discussed in Section 6.2.

Selected area electron-diffraction (SADP) in the TEM was also used to examine specimens SI101, SI108 and AY1, AY2 and AY6. Again the results are shown in Table I. By comparison with the ECP results, this technique enables highly damaged material to be distinguished from completely amorphous material. Thus, while AY6 was found to have an amorphous surface, AY2 was found to be crystalline but damaged. In general, correlation of the RBS, ECP and TEM results usually allows the state of the sample surface to be determined unambiguously (see Section 6.2). The estimated dose for the onset of amorphization has enabled a critical energy deposition amorphization criterion to be determined for sapphire as shown in the Appendix.

Specimen AY6 was of particular interest as the surface of the specimen showed a "crazing" after implantation, as did specimens AY4 and AY5. Figs. 4a and b shows SEM micrographs of this surface in both secondary and backscattered imaging modes and it may be seen that the crazes appear dark in backscattered mode. This could indicate that the mean atomic number of the material at the bottom of the crazes is lower than that of the surrounding raised regions, i.e. that the crazes have a low yttrium content and are essentially where the amorphous layer has been torn open to reveal the material of lower implant concentration below. Fig. 4c is a transmission electron micrograph, together with SADPs, of AY6 taken across a crazed region and it may be seen that the crazes are crystalline and the raised regions amorphous. Thus, the implication is that the crazes arise from tearing of the surface amorphous layer in response to implantation-induced stresses. In this case the surface is placed in tension by expansion of sub-amorphous layer material to accommodate the "ion stuffing" effect associated with the deposition profile (see Section 6.3).

4. Indentation fracture and plasticity

Lawn, Evans and co-workers [10–13] have attempted to quantify both the stress fields that give rise to fracture around Vickers indentations in brittle materials together with the characteristic crack morphologies which result. As shown in Fig. 5, generally there are two distinct types of crack formed: (a) "penny-like" median cracks which form during loading and grow up to the surface on unloading to form a radial crack array, and (b) lateral cracks formed on unloading under the influence of residual tensile stresses in the near-surface region. The lateral cracks are believed to grow from the elastic/plastic boundary of the enclave of plastically deformed material immediately below the indenter, e.g. [14].

In the sections that follow, the trajectories and

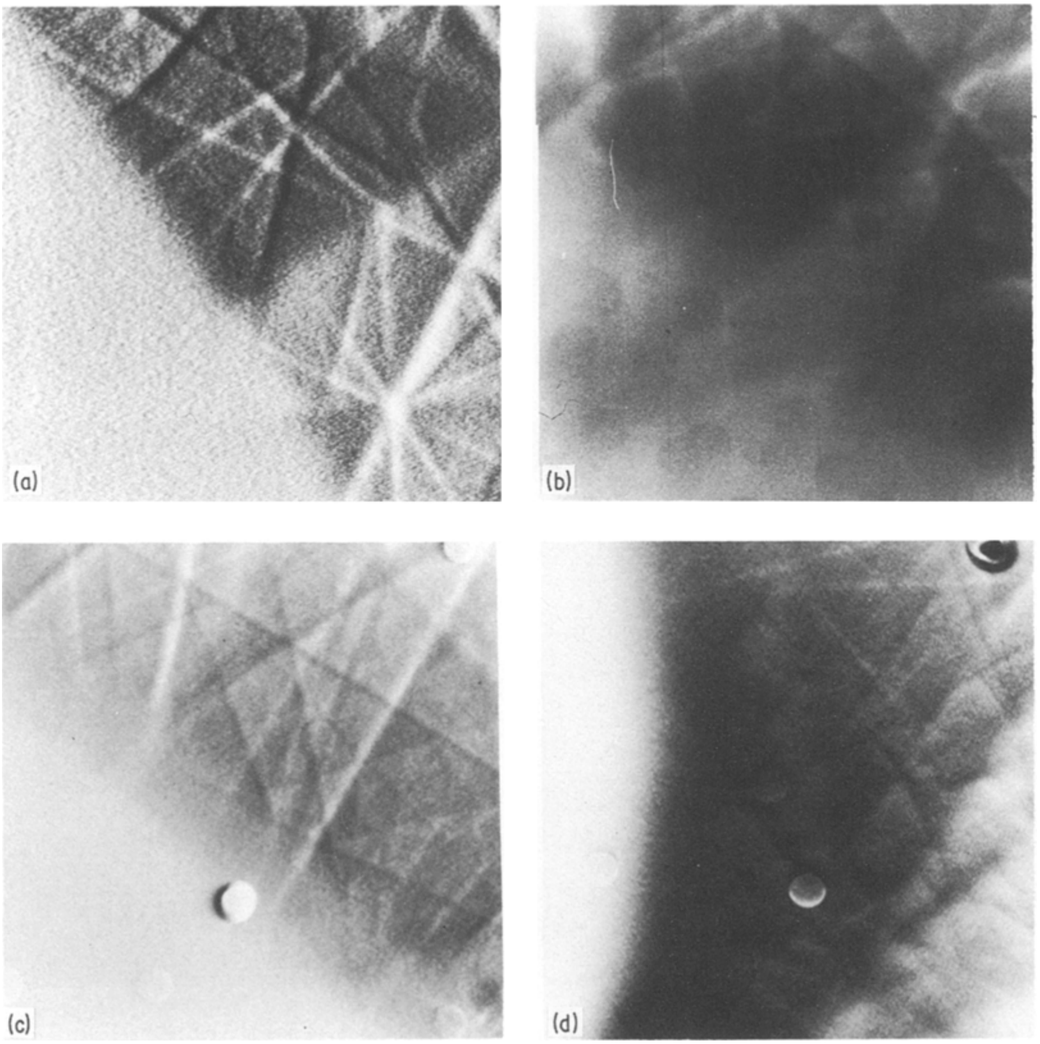

Figure 3 Wide area electron channelling patterns (WACP) spanning the implanted/unimplanted boundary obtained in an SEM (backscattered electron imaging mode; annular solid state detector) operating at 30 keV with a working distance of ~ 10 mm and an overfocus of ~ 134 mm. (a) SI21, implanted region amorphous, no channelling; (b) AY2, implanted region damaged but still crystalline, pattern still present but degraded; (c) AY3, RBS had indicated that a surface crystalline layer may be present (Fig. 2b) but channelling contrast disappeared on crossing the implanted/unimplanted boundary; (d) AY6 implanted region amorphous, no channelling. Note the strong atomic number contrast between the Y-rich implanted region and the unimplanted material. Contrast was enhanced in (a), (c) and (d) using a derivative signal processing unit. The insulating sapphire specimens were lightly gold coated (~ 25 nm) prior to channelling.

extent of both radial and lateral cracks in the unimplanted control specimens are characterized and the modifications to the fracture behaviour by ion implantation described. Finally, some observations on the plasticity of the ion-implanted surfaces are made.

4.1. Radial fracture

The fracture around Vickers indentations in single crystal brittle materials is strongly influenced by crystallography, i.e. the orientation of the planes of easiest cleavage with respect to the tensile components of the indentation stress field. For both the $\{111\}$ section silicon and the $\{10\bar{1}2\}$ section sapphire used in this study, there are preferred cleavage planes normal or near-normal to the test surface. From the cubic stereogram of Fig. 6a, it may be seen that (111) silicon may be

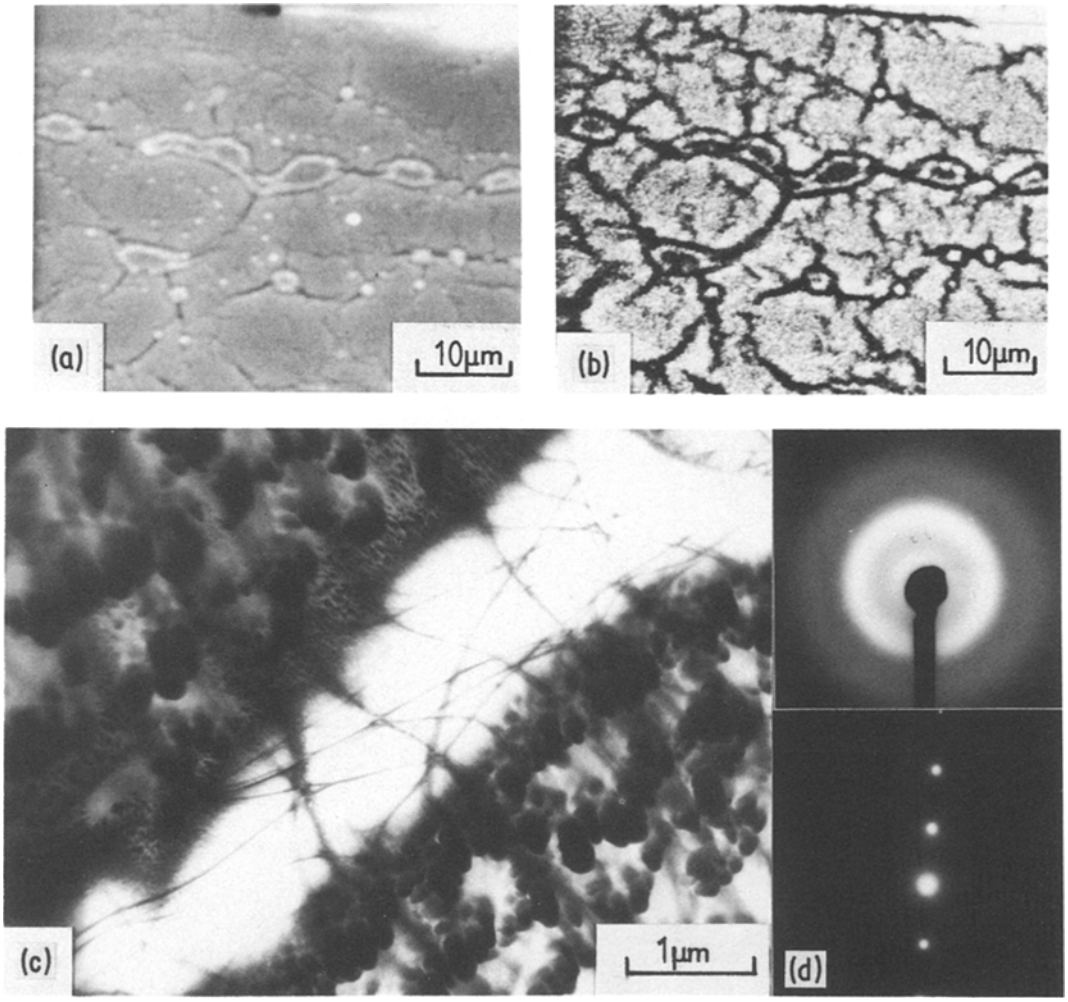

Figure 4 (a) Secondary and (b) backscattered (annular solid state detector) SEM images of the "crazed" surface of AY6. The strong contrast in (b) is probably due to atomic number differences, resulting from the lower Y content of the material revealed by crazing. (c) A TEM micrograph (100 kV) across a "craze" (the specimen was prepared by "back-thinning" a 3 mm disc cut from a region of AY6). Convoluted bend contours may be seen within the craze indicating that this region of the specimen was highly stressed. The upper diffraction pattern was obtained from the material on either side of the craze and shows diffuse rings characteristic of amorphous material. The lower diffraction pattern was obtained from the bottom of the craze and shows it to be crystalline.

expected to crack on the $\{0\bar{1}1\}$ planes normal to the surface (i.e. those contained within the $[111]$ zone) and possibly also on those $\{111\}$ planes inclined at 70° to the surface. These possible crack planes produce $\langle 1\bar{2}1\rangle$ and $\langle 1\bar{1}0\rangle$ traces at regular 30° intervals as shown in Fig. 6b. Fig. 7a is a similar stereogram for sapphire (α-Al_2O_3: hexagonal, $c/a = 2.73$) and Fig. 7b shows that the expected cleavage planes normal and near-normal to the surface produces a pattern of median/radial crack paths at ~ 45° and ~ 90° to each other. Figs. 8 and 9 show Vickers indentations in both implanted and unimplanted silicon and sapphire. It may be seen clearly that the principal cracks in silicon lie along the $\langle 1\bar{2}1\rangle$ directions* (i.e. the traces of the $\{0\bar{1}1\}$ planes perpendicular to the test surface) and that the $\{111\}$ planes at 70° to the surface show little evidence of cracking. For sapphire, cracking on both the $\{10\bar{1}2\}$ and $(1\bar{2}10)$ planes normal to the surface may be seen,

---

*As has been reported by Puttick and Hosseini [15], these $\langle 1\bar{2}1\rangle$ cracks are usually unexpectedly asymmetric in that they extend principally from one side of the indentation only. No clear explanation has been reported for this phenomenon.

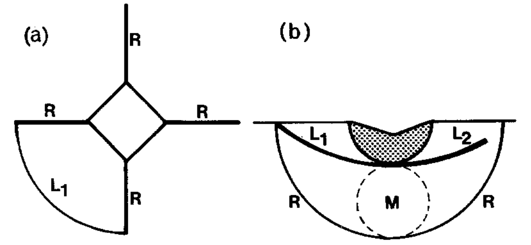

Figure 5 A schematic representation of the crack geometry around a hardness indentation in a brittle sample, (a) plan view and (b) profile. M is the "penny-like" median crack formed during loading and R its radial extension formed in response to the residual tensile stresses during unloading. Lateral cracks L_1 and L_2 also form during unloading and may (L_1) or may not (L_2) reach the surface.

with the appearance of only one 45° crack as is predicted by the stereogram of Fig. 7. Consideration of Figs. 8 and 9 shows that ion implantation apparently has little or no effect upon radial crack trajectories or upon the incidence of radial cracking. However, in Fig. 10a, where the indentations have been broken open along the radial cracks, the semi-circular trace of the radial crack in unimplanted silicon may be seen. By comparison, Fig. 10b shows the trace of the radial crack in the implanted silicon and this now appears oblate or elliptical, the radial crack narrowing towards the surface. Fig. 10c shows a further example of this effect where the radial/median crack has extended proportionately further but still shows the backward deflection at the surface. These observations suggest that the compressive stresses introduced by implantation are responsible for the shortening of the traces of the radials on the test surface and this may affect K_{IC} values calculated from indentation crack lengths (see Section 6.3).

Using a Leitz "Miniload" with a Vickers profile indenter, the load dependence of the lengths of both indentation diagonals and radial cracks was measured, under ambient conditions, for five indentations at loads of 500 gf and 200 gf for specimens SU101, SI102 and SI21.* Lawn and co-workers [10–13] have derived relations linking radial crack growth to the indentation stress fields that occur during and remain after indentation. The modifications to the stress field due to the sub-indenter plastically deformed zone have been

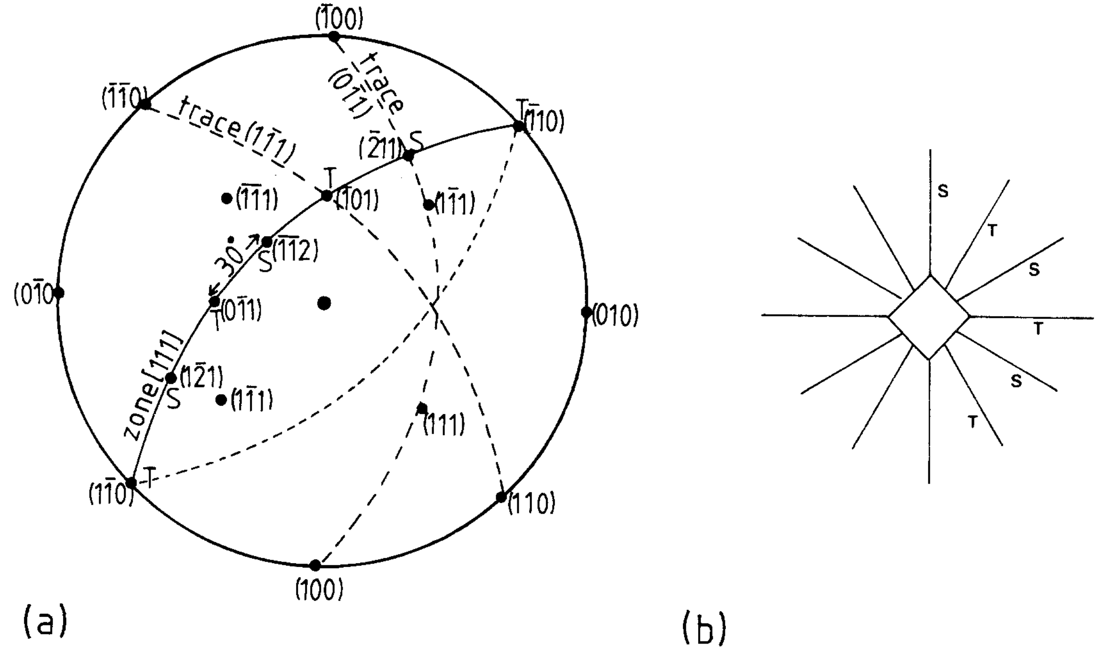

Figure 6 (a) Stereogram of silicon (cubic F lattice) showing the crystallography of possible median/radial crack systems. For a (111) test surface, three of the $\{110\}$ cleavage planes are perpendicular to the surface and produce $\langle 1\bar{2}1\rangle$ crack traces, S. The three remaining $\{111\}$ planes are inclined at ~ 70° to the surface and may possibly crack during indentation. On the (111) surface, these planes would result in $\langle 1\bar{1}0\rangle$ crack traces and are marked T. (b) When viewed on the (111) surface, traces S and T produce regular traces at 30° to each other.

*An attempt was made to measure the crack lengths around indentations in specimen SI108 but poor contrast due to the surface sputtering caused by implantation made this impossible.

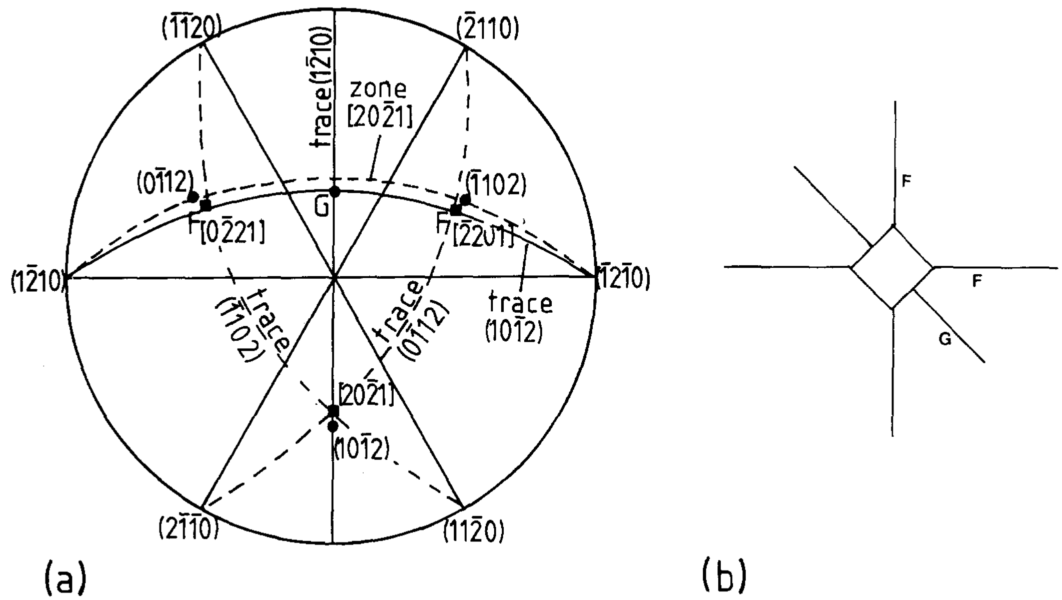

Figure 7 (a) Stereogram of α-Al_2O_3 (hexagonal, $c/a = 2.73$) showing the crystallography of possible median/radial crack systems. For a $(10\bar{1}2)$ test surface, only one of the $\{2\bar{1}\bar{1}0\}$ cleavage form (i.e. $(1\bar{2}10)$) is perpendicular to the surface and produces a $[10\bar{1}\bar{1}]$ crack trace G. Of the $\{10\bar{1}2\}$ cleavage form, both $(0\bar{1}12)$ and $(\bar{1}102)$ are very nearly perpendicular to the test surface producing the near-orthogonal $\langle\bar{2}201\rangle$ traces F. (b) When viewed on the $(10\bar{1}2)$ surface, traces G and F produce intercrack angles of ~ 45° and ~ 90°.

discussed by Evans [12] and from this a more appropriate description of the forces on the cracks has been proposed, leading to better K_{IC} values. Using the relation derived by Lawn and co-workers [10–13]*

$$K_{IC} = 0.0139(E/H)^{1/2}PC_r^{-3/2} \qquad (1)$$

[where H is the Vickers hardness (kgf mm^{-2}), E is the Young's modulus (GPa), P is the applied load and C_r is the radial crack radius] the fracture toughness (K_{IC}) for each specimen at each load was calculated. Similar tests were performed upon specimens AU1, AY2 and AY6 at loads of 1000 gf and 200 gf and the K_{IC} values determined. The results of these analyses are presented in Table II. In general, it may be seen that the fracture toughness of both silicon and sapphire apparently increases after implantation and that the magnitude of the increase is greater at lower loads.

4.2. Lateral fracture

Theoretical determination of the exact trajectories, position and extent of lateral cracks is difficult, although Marshall *et al.* [18] have made some progress towards describing the phenomenon.

Lateral fracture becomes particularly important in erosion and wear processes where lateral crack break-out combined with radial cracks can lead to substantial material removal, e.g. [14]. Roberts and Page [3] have reported that ion implantation of silicon and silicon carbide can inhibit lateral crack break-out or even suppress crack genesis.

TABLE II Indentation fracture toughness

Specimen	Dose (ions cm^{-2})	Fracture toughness, K_{IC} (MPa m$^{1/2}$)		
		200 g	500 g	1000 g
SU101	0	0.744	0.886	–
SI102	2×10^{17} Al^+	0.961	1.041	–
SI21	5×10^{17} Al^+	1.291	1.191	–
AU1	0	1.081	–	1.696
AY2	0.2×10^{17} Y^+	1.451	–	1.530
AY6	5.8×10^{17} Y	1.502	–	1.693

---

*Since we are only interested in relative changes in fracture behaviour, this equation rather than its later forms (e.g. [16, 17]) has been used.

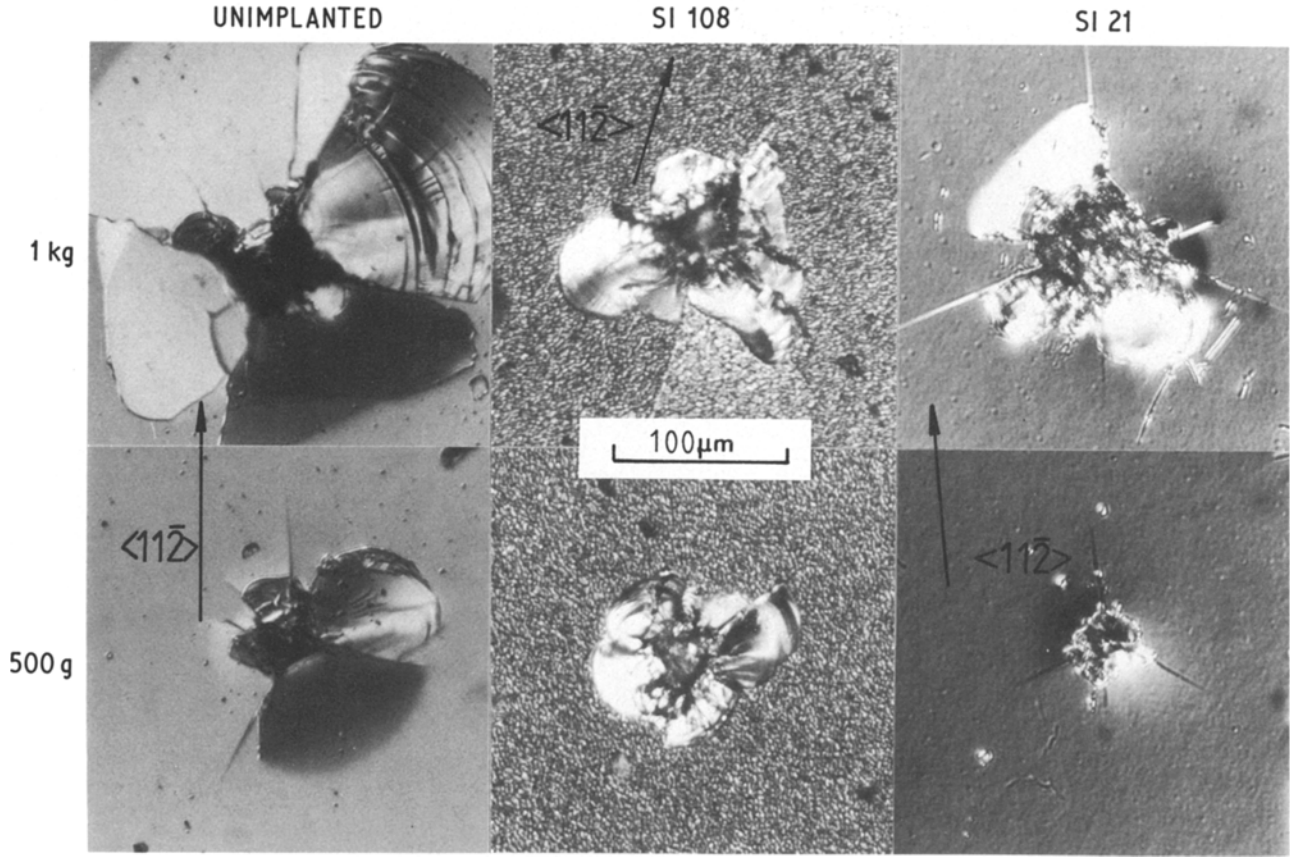

Figure 8 Nomarsky interference micrographs of Vickers indentations (at loads of 1 kgf and 500 gf) on silicon specimens SI108, SI21 and SU101 (unimplanted). Note the presence of radial cracks 120° apart along the $\langle 1\bar{2}1\rangle$ directions. Lateral break-out is much reduced after implantation. The sputtered surface topographies of SI108 and SI21 were induced by *implantation.*

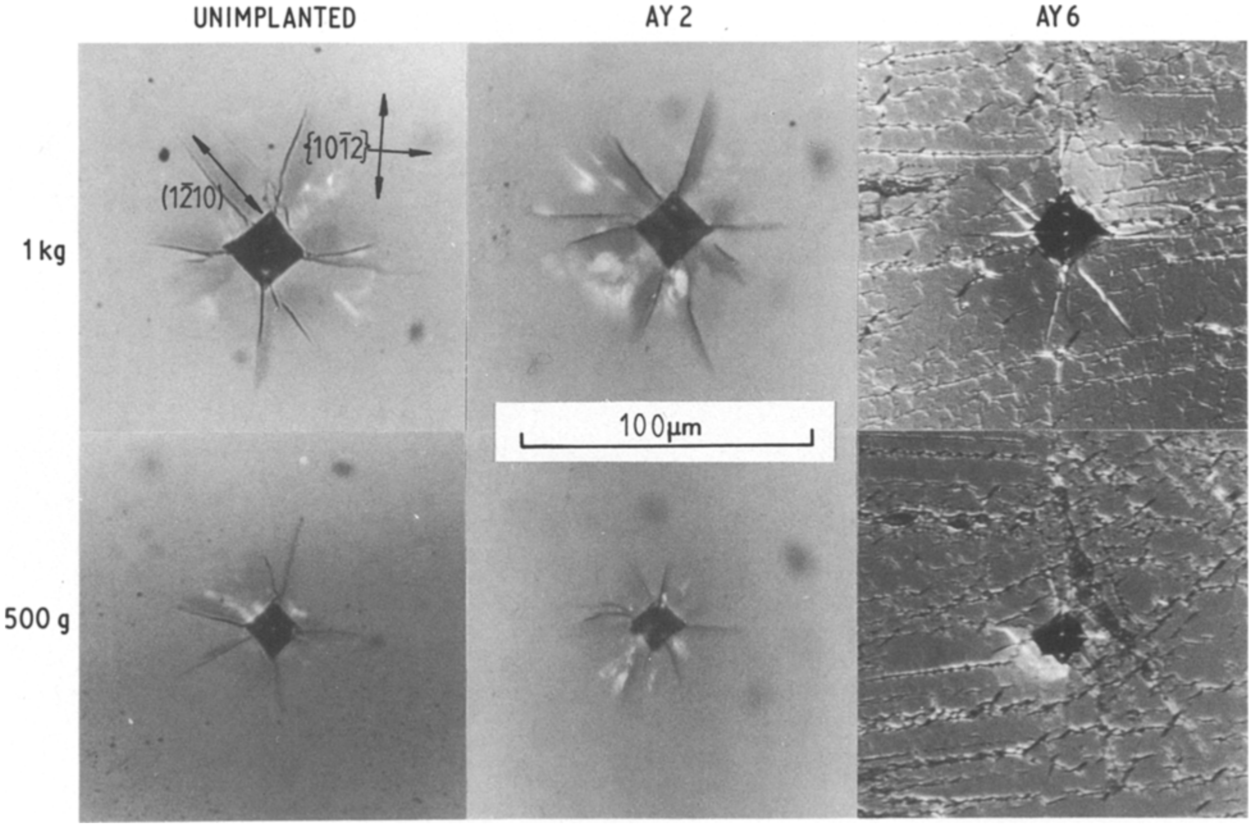

Figure 9 Nomarsky interference micrographs of Vickers indentations (at loads of 1 kgf and 500 gf) on sapphire specimens AY2, AY6 and AU1 (unimplanted). Note the presence of the $\{10\bar{1}2\}$ crack traces (approximately vertical and horizontal) together with the $(11\bar{2}0)$ crack trace at ~ 45° to the other cracks. There is no lateral break-out. The surface of AY6 shows crazing.

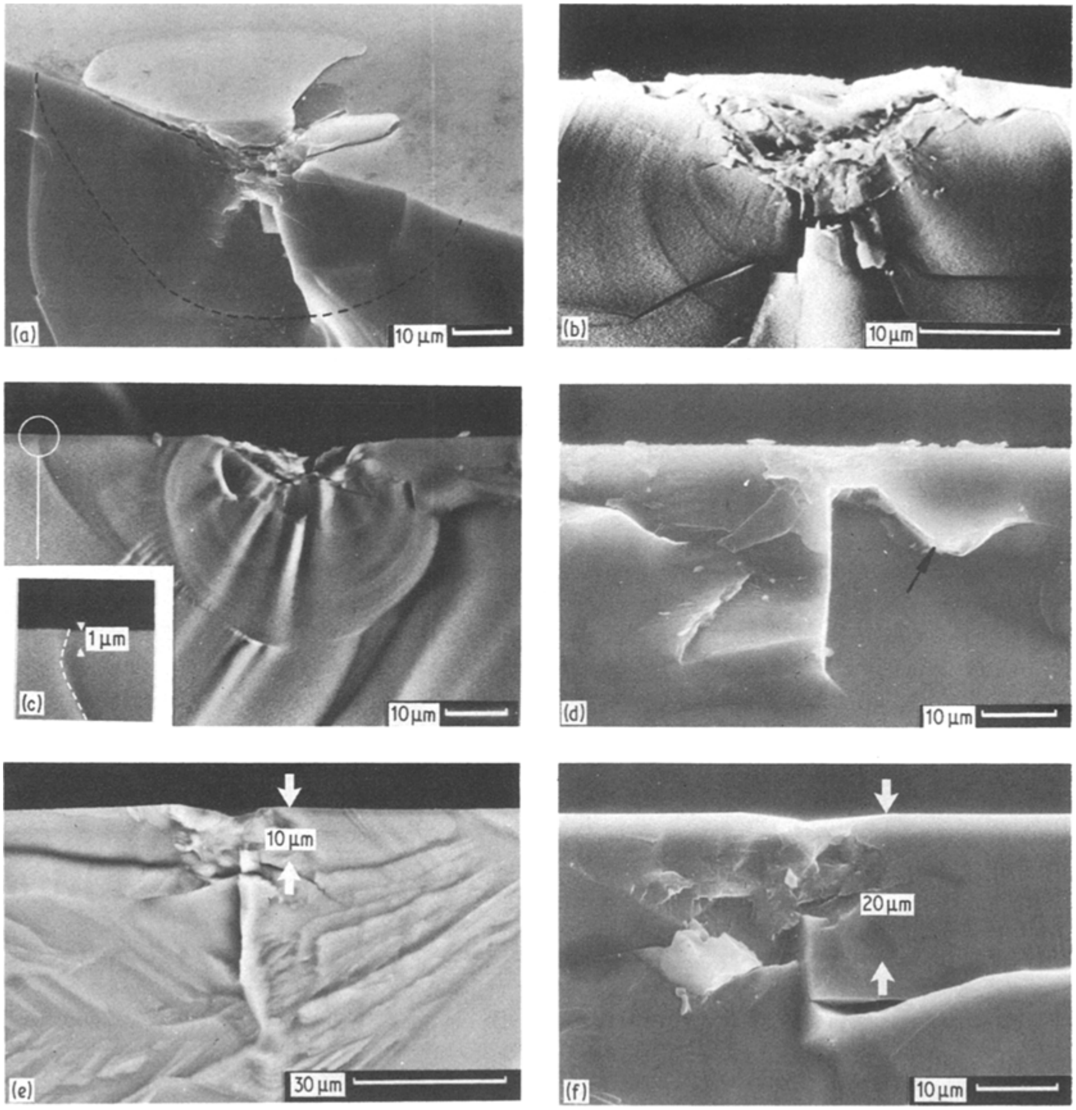

Figure 10 Scanning electron micrographs of Vickers indentations broken open along the lines of their radial cracks. (a) 300 g, unimplanted silicon showing lateral break-out and the traces of the progressive extension of the median/radial crack system finally resulting in the semicircular (approximately) radial crack marked (secondary electron image). (b) 300 g, SI21, showing lateral cracks lying far deeper than those of (a) and running parallel to the surface. Note the rather more oblate appearance of the radial crack traces in this case (backscattered electron image, derivative processing). (c) 300 g, SI21, showing the alteration of the final radial/median crack trace by the compressive stresses within the implanted layer (~ 1 μm thick). Note the almost complete suppression of lateral fracture in this case (backscattered electron image). (d) 300 g, SI108, showing the deflection (arrowed) of lateral cracks upon approaching the surface (secondary electron image). (e) 500 g, unimplanted sapphire showing the more typical occurrence of lateral cracks in sapphire ~ 10 μm beneath the surface (backscattered electron image). (f) 500 g, AY6, showing lateral cracks occurring at greater depth than in (e). The sapphire specimens were lightly gold coated prior to imaging.

Fig. 8 shows this effect for specimens SI108 and SI21; it can be seen that lateral break-out and surface lifting (due to sub-surface lateral cracks) is considerably reduced after implantation, and that where break-out does occur it is substantially closer to the centre of the indentation. For sapphire, lateral break-out is a rare occurrence, even under 1000 gf indentation. Fig. 9 shows no break-out for either the implanted or unimplanted specimens. However, since sapphire is transparent, it is possible to view the sub-surface cracking using reflected polarized light microscopy, e.g. [19]. In Fig. 11, it may be seen that the extent and number of lateral cracks produced by 1000 gf indentation

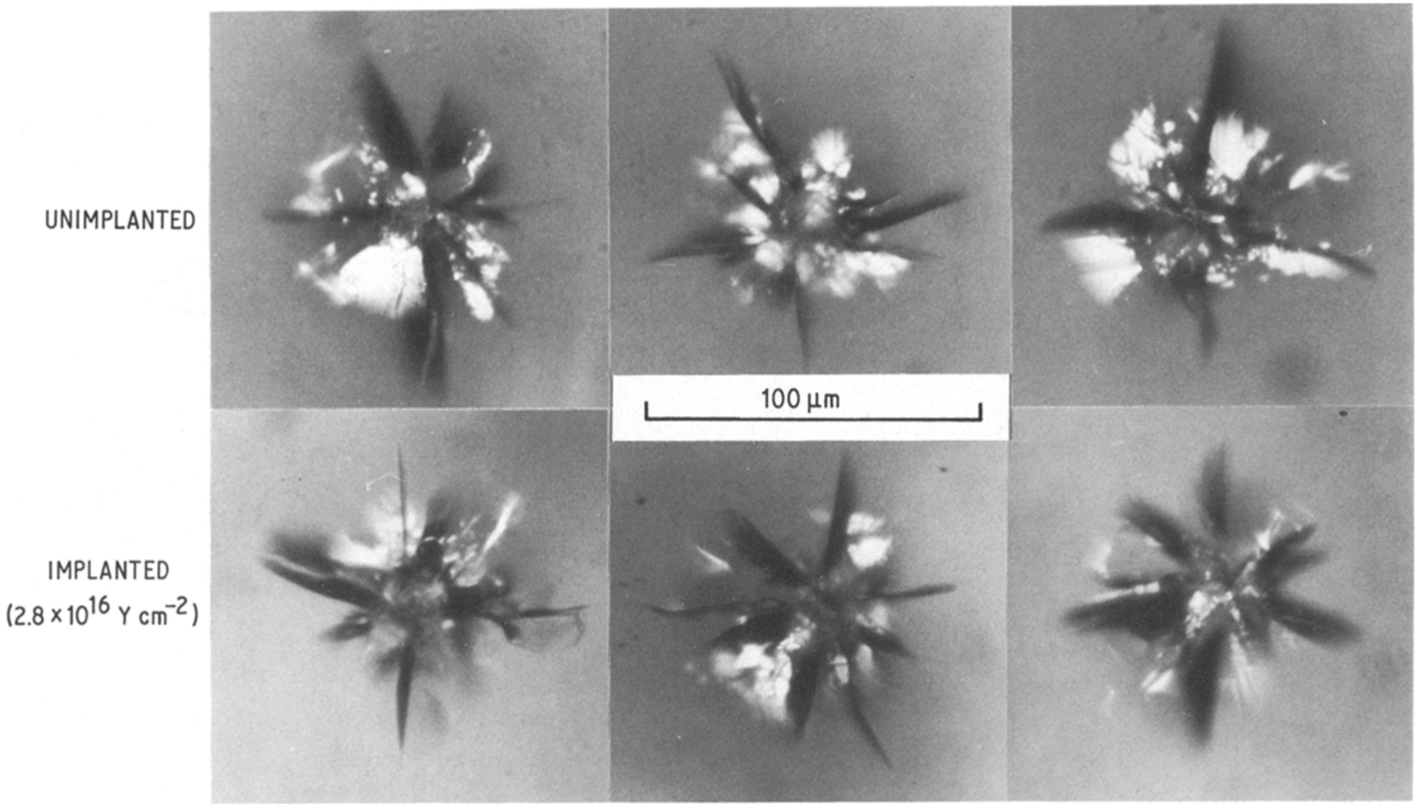

Figure 11 Reflected polarized light micrographs of 1 kgF Vickers indentations on unimplanted and implanted (2.8×10^{16} $Y^+ cm^{-2}$; AY2) sapphire showing the position and extent of the sub-surface lateral cracks. These cracks are generally smaller and less numerous in the implanted material and have somewhat lower levels of contrast possibly indicating that the cracks lie further beneath the surface than for the unimplanted case.

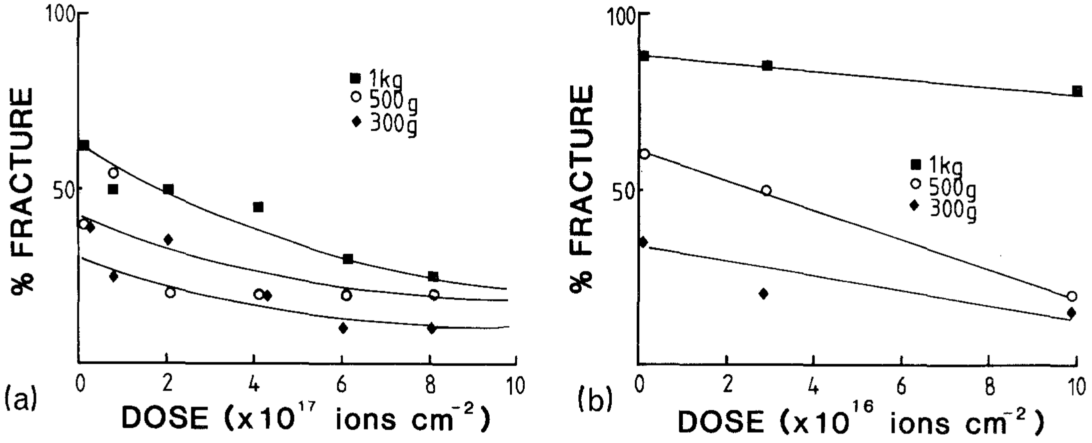

Figure 12 (a) The frequency of occurrence of lateral breakout after Vickers indentation of N$_2^+$ implanted silicon showing the decrease in break-out after implantation. (b) The frequency of occurrence of sub-surface lateral fracture in Y$^+$ implanted sapphire showing slight decreases in lateral fracture at 1 kgf and 300 gf and a more marked decrease after indentation at 500 gf (see text for method of percentage fracture calculation).

on AY2 is reduced after implantation and, notably, at a dose below that required for the onset of amorphisation.

Fig. 12 is a semi-quantitative description of the variation of lateral fracture with dose for both silicon and sapphire. To calculate "percentage-lateral fracture", the region around the indentation was divided into four quadrants and the fraction of quadrants in which fracture occurred determined. In order to have some standard, "fracture" was arbitrarily defined as lateral break-out for silicon and the presence of a substantial sub-surface lateral crack for sapphire (the criterion taken was that the lateral crack should extend further than one quarter of the radial crack's length). Five indentations were considered at each load for each specimen. The observed trend is that increasing the dose decreases the percentage fracture.

Scanning electron microscopy of indentations broken open along the line of their radial cracks (Fig. 10) showed that ion implantation not only resulted in less lateral cracking but also in the lateral cracks sometimes being formed further from the surface. Their trajectories, whilst being dominated by the cleavage crystallography of the material, may also be seen to differ. Thus, while lateral cracks in the implanted material may generally be seen to run parallel to the surface (Fig. 10b), those running towards the surface will often appear to be deflected away from the surface on close approach (e.g. Fig. 10d). These observations indicate a difference between the residual stress field remaining after indentation in an implanted specimen and that in an unimplanted specimen. A further effect of implantation on lateral crack behaviour is shown in Figs. 10e and f, where the cracks in alumina are found to lie at increased depths after implantation. Again, implantation induced stresses are presumed to be responsible.

4.3. Plasticity

Although the indentation fracture behaviour remains characteristically brittle both before and after implantation, the shape of the indentations differs. In Figs. 8 and 9 it may be seen that, while indentations in most specimens appear "pin-cushioned" in shape, there is some hint that those in the highest dose specimens are becoming "barrelled". This barrelling is caused by part of the indentation lying in the plastically "piled-up" material displaced by the indentation process, e.g. [20]. This can be seen more clearly in Figs. 13 and 14. These are SEM stereopairs of low load indentations which, when viewed with a stereoviewer, show the ridges formed by pile-up confirming this explanation. Also included in Figs. 13 and 14 are near edge-on (~ 80° tilt) SEM micrographs of the same indentations clearly showing the same piled-up material standing proud of the original surface. Similar pile-up was apparent in specimens SI106–8 and AY4, 5 (which also showed crazing) but not in the lower dose N$_2^+$ or Y$^+$ implanted specimens. The RBS results of Section 3 would seem to indicate that the increased plasticity of the surface is allied to the production of an amorphous layer and that only the specimens with the thicker layer show substantial amounts of pile-up

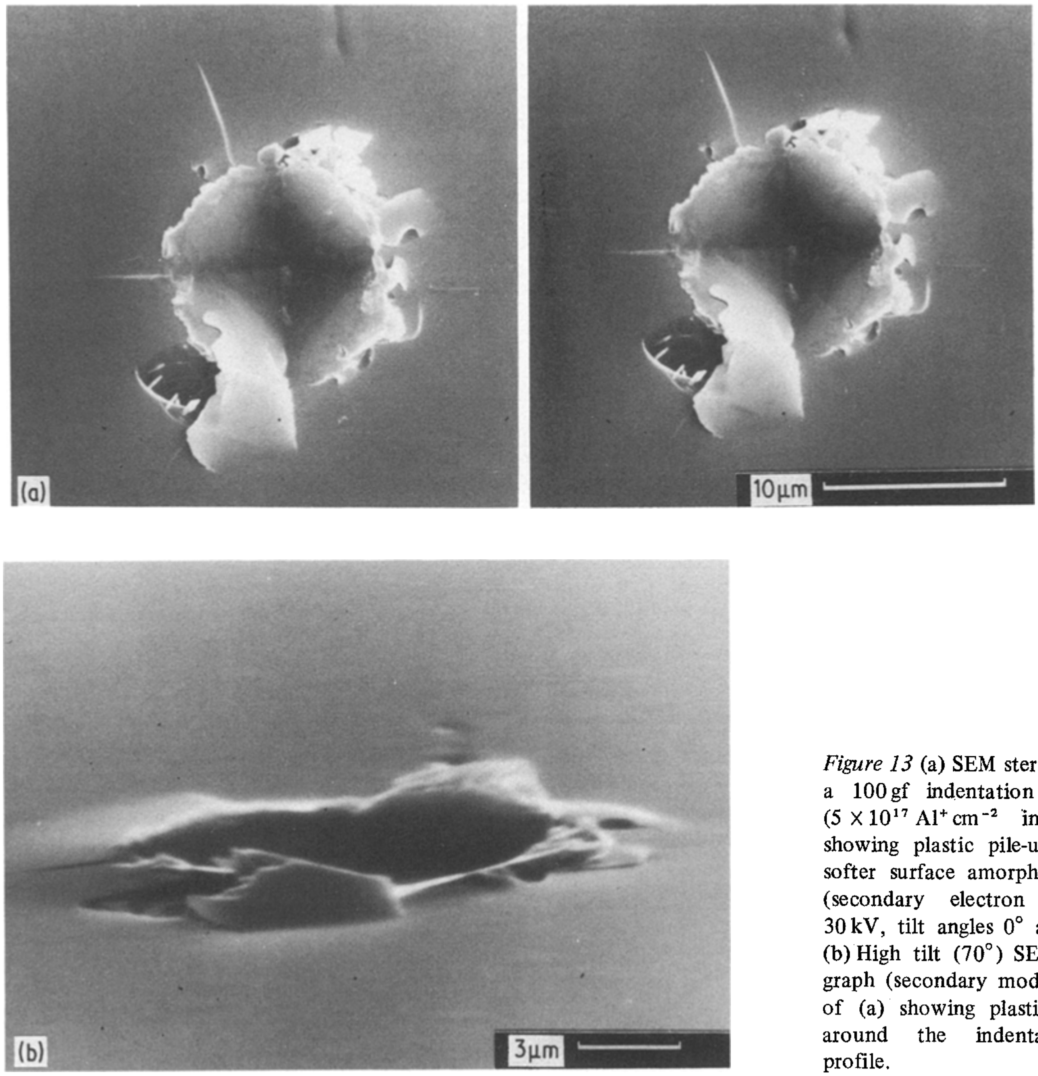

Figure 13 (a) SEM stereo pair of a 100 gf indentation in SI21 (5×10^{17} $Al^+ cm^{-2}$ in silicon) showing plastic pile-up of the softer surface amorphous layer (secondary electron imaging, 30 kV, tilt angles 0° and 10°). (b) High tilt (70°) SEM micrograph (secondary mode; 30 kV) of (a) showing plastic pile-up around the indentation in profile.

at the scale of indentation and observation used here.

5. Hardness

The effect on hardness of N_2^+ ion implantation into silicon has been discussed more fully in previous work [3, 4] but some of the data from [4] will also be presented here to enable comparisons with the new work on Y^+ implanted sapphire to be made.

Room-temperature microhardness tests (under ambient conditions) at loads of 25 gf were performed on the silicon using a Leitz "Miniload". A Vickers profile indenter was used and aligned such that one diagonal was parallel to the $\langle 1 1 \bar{2} \rangle$ direction and the other to the $\langle 1 \bar{1} 0 \rangle$ direction (see Fig. 6). Constant lighting conditions were maintained throughout the testing (artificial light in a darkened room) and a standard loading cycle time of 25 sec was used for each test to minimize the effect of indentation creep on hardness.

Five indentations per specimen were made (giving ten diagonal measurements in all) and the hardness evaluated from the mean diagonal size. Each testing session consisted of the testing of at least two specimens (including an unimplanted control) consecutively. It was thus hoped to minimize the effect of variation in operator performance between sessions.

Knoop microhardness tests were performed upon the sapphire specimens. Since the diagonal: depth ratio of the Knoop indenter is 30.5 : 1, compared to that of 7 : 1 for the Vickers indenter, it was felt that, due to the much shallower depth of the implanted layer in these specimens (see Table I), this geometry would allow rather more

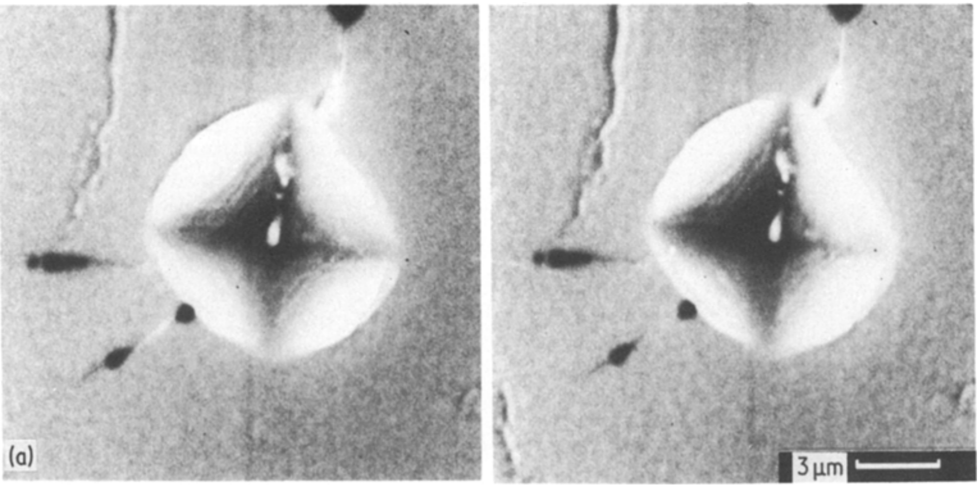

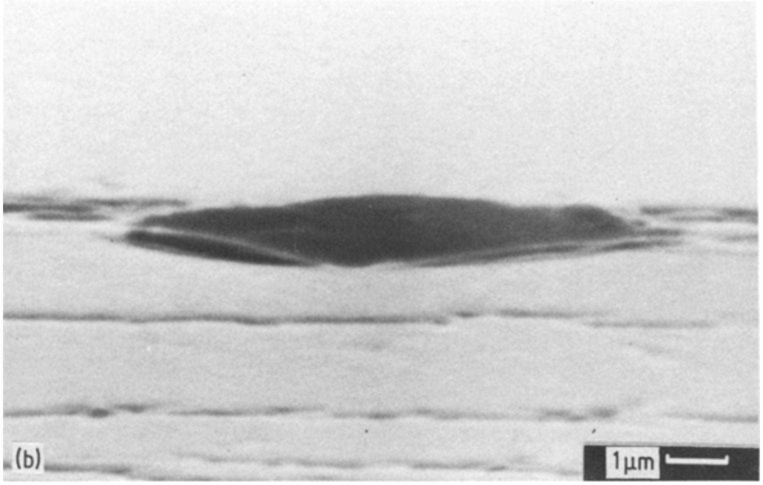

Figure 14 (a) SEM stereo pair of a 100 gf indentation in AY6 (5.7×10^{17} $Y^+ cm^{-2}$ in sapphire) showing plastic pile-up of the softer surface amorphous layer (secondary electron imaging, 30 kV, tilt angles 0° and 10°). (b) High tilt (80°) SEM micrograph (secondary mode; 30 kV) of (a) showing plastic pile-up around the indentation in profile.

accurate monitoring of any changes in the hardness of this thin ($< 0.3\,\mu m$) layer. The major disadvantage incurred by using a Knoop profile indenter is the increased sensitivity to hardness anisotropy effects, e.g. [21], so additional care was taken to ensure that the long diagonal of the indenter was always aligned along one of the $\langle 20\bar{2}1\rangle$ directions. Six indentations each at loads of 25 gf and 50 gf were made on each specimen, all other testing conditions being as for the silicon tests.

The variations of hardness with dose for both silicon and sapphire are presented in Figs. 15 and 16 together with the predicted and experimental variations of amorphous layer thickness with dose. As has been described in detail elsewhere [4], the 25 gf hardness of N_2^+ implanted silicon may be seen to decrease rapidly when a rapid rise in amorphous layer thickness occurs. Fig. 16 shows a similar layer-thickness dependence of hardness for Y^+-implanted sapphire, the hardness decreasing upon the initial formation of the amorphous layer and then decreasing further as the layer thickens. It should be noted that this latter change occurs in conjunction with the formation of the crazed surface of specimens AY4, AY5 and AY6. The mechanism of formation of the crazing is as yet unclear, but as discussed in Section 3, it is thought to be induced, or at least assisted, by the high implantation stresses present in the surface tearing the softer and more ductile amorphous layer.

In Fig. 16, the specimen with the lowest dose Y^+ implant (AY1) shows a significant increase in hardness. Similar hardening has been observed by us for other species implanted into Al_2O_3, the hardening always occurring at doses below those necessary for any amorphization [22]. This effect is attributed to either solid solution and/or radiation hardening (see Section 6.4).

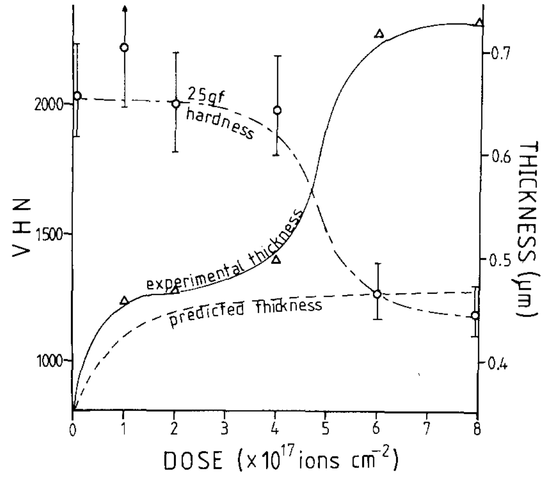

Figure 15 The variation with dose (N_2^+ into silicon) of 25 gf Vickers hardness and both experimental and predicted amorphous layer thicknesses. Note the correspondence between the rapid fall in 25 gf Vickers hardness and the rapid increase in amorphous layer thickness. The error bars for the 25 gf hardness are 2σ.

6. Discussion

Sections 3, 4 and 5 have presented results showing the effects of ion implantation upon the structure, hardness and near-surface fracture behaviour of both silicon and sapphire. The dose sensitivity of these effects has also been established. Further, the Appendix shows how a critical energy deposition level for amorphizing sapphire can be estimated. For the observed changes in plasticity and fracture behaviour, broad distinctions have been drawn between the possible controlling influences of the damaged surface layer and the implantation-induced stresses. From these results, a number of points require further comment and this discussion, for convenience sub-divided by topics, now follows.

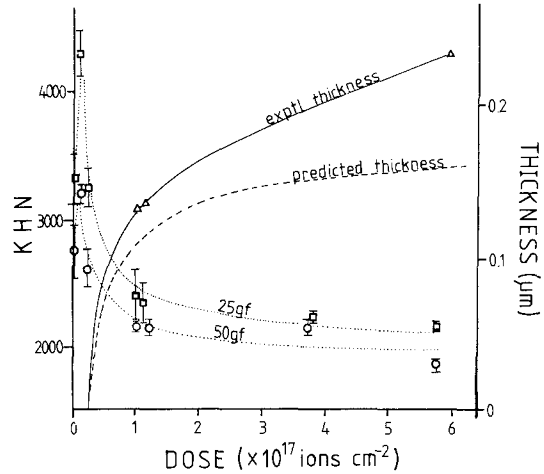

Figure 16 The variation with dose (of Y^+ into sapphire) of □ 25 gf Knoop hardness, △ 50 gf Knoop hardness, and both predicted and experimental amorphous layer thicknesses. Note the initial increase in hardness (presumed due to either solid solution hardening and/or radiation hardening) followed by a drop in hardness at the onset of amorphization ($\sim 3 \times 10^{16}\,Y^+\,cm^{-2}$). The hardness continues to fall as the layer thickness increases. Note also that, as for silicon, the experimental amorphous layer thickness deviates markedly from that predicted at high doses. The error bars for the hardnesses are 2σ.

6.1. Choice of ion species/energies

Nitrogen implantations into silicon were investigated to further clarify the previous work of Roberts and Page [3] in which surface softening and inhibition of lateral fracture were first reported. 300 kV Al^+ was chosen as an alternative implant species into silicon because, although both the projected range of these ions is greater than for N_2^+ and the atomic mass of Al is greater than that of N (leading to more displacements per ion), the amorphous layer produced at doses of $5 \times 10^{17}\,Al^+\,cm^{-2}$ is comparable in scale and damage with the unexpectedly thick layers produced by high dose (6 to $8 \times 10^{17}\,ions\,cm^{-2}$) implantations of N_2^+. This is shown in the experimentally determined layer thicknesses in Table I. In addition, these two species allow the effect of implant valency upon the mechanical properties of silicon to be explored and this has been reported elsewhere [4].

Yttrium is nominally isovalent with aluminium in sapphire and is one of a range of ion species being implanted into sapphire in the current research programme. The energy (300 keV) of the ion beam was chosen principally because of the need to produce reasonable ion currents (~ 2 to $3\,\mu A\,cm^{-2}$) in order to minimize machine implantation time, while still resulting in an amorphous layer of reasonable thickness.

6.2. Surface damage and amorphization

TEM was the technique of first choice for extracting detailed structural information from the implanted layer. The use of specimens prepared using plan and cross-sectional preparation routes can yield a wealth of information on sub-surface disorder and deformation. However, sophisticated specimen preparation, such as that needed to obtain foils cross-sectioning the damaged layer, is tedious, time-consuming and may have a high failure rate. Consequently, a range of complementary techniques have been used in an attempt to unravel the structural changes taking place during implantation. RBS can reveal the shape of the implant profile and, when a channelled technique is used, quantitative information about the distribution of displacement damage may also be obtained (e.g. [7]).

The onset of amorphization (or extreme disorder) is always clearly seen using electron diffraction. However, it was found that higher damage levels were necessary to change channelled RBS spectra into the unchannelled spectra expected for amorphous material. Further, there is no correlation between the damage levels for amorphization as monitored by these two techniques. Thus TEM was always used to help interpret the RBS spectra.

Electron channelling patterns (ECP) obtained in the SEM may provide instant confirmation that a surface (to a depth of ~ 100 nm [8]) is both crystalline and fairly perfect. However, the absence of an ECP does not necessarily mean that the surface is amorphous, merely sufficiently disordered to render the ECP undetectable. Davidson and Booker [9] have demonstrated this degradation of channelling pattern quality with increasing dose of Ne^+ into silicon. In the current programme complete disappearance of 30 kV ECPs occurred near to the onset of amorphization of both Si and Al_2O_3 but below the amorphization dose of MgO [23]. In addition implantation-induced stresses may also result in strains within the surface which will further degrade the channelling pattern quality. Thus ECPs are a useful but neither infallible nor sensitive monitor of surface amorphization.

Thus, in summary, a combination of TEM, RBS and ECP usually allows an unambiguous determination of the surface microstructural state as shown in Table I.

Clearly, the exact value assigned to the critical energy criterion for amorphization (CECA) of sapphire is dependent upon the correct interpretation of the data obtained from the microstructural techniques. In the dose range studied here, the amorphous layer thickness–dose behaviour predicted for silicon is fairly insensitive to the value of CECA assumed (see Fig. 1 and [4]), the lack of sensitivity arising from the doses all being well above the onset of amorphization and the thickness–dose curves having a small slope in Region III in Fig. 1. However, for sapphire, amorphization first occurs in the dose range studied, and the thickness of the amorphous layer is expected to vary rapidly over this range (Region II in Fig. 1). Consequently the value of CECA assumed can markedly alter the predicted layer thickness. However, the CECA value derived in the Appendix allows good correlation between the microstructural observations and the hardness behaviour.

6.3. Fracture behaviour and implantation-induced stresses

In Section 4 it has been shown that ion implantation can affect indentation fracture behaviour both by modifying the morphology of lateral fracture and decreasing the extent of radial crack breakthrough at the surface. In general, these effects are observed to occur before the onset of amorphization, suggesting that both phenomena are a result of implantation-induced stresses rather than amorphization. In this study, this behaviour is exemplified by specimen AY2 but similar behaviour has been observed for a range of brittle materials in both this project and work elsewhere [22–25]. After amorphization the implantation-induced stresses can result in the crazing behaviour also reported in Section 3.

Most workers assume that the stress state is principally one of localized biaxial compression in the plane of the surface, e.g. [26]. In massive samples, lateral expansion is constrained by the underlying substrate. However, in thin samples the stresses can result in detectable bending, e.g. [26], as in the Si and Al_2O_3 wafers used here. Beneath the surface, the stress state is probably nonuniform and might be expected to reach a maximum somewhere around the peaks of the damage and concentration profiles. The situation is further complicated by the varying disorder/composition beneath the surface which will affect the mechanical properties, e.g. elastic constants.

For sapphire, the possible maximum magnitude of the stress (in the dose range investigated here) can be estimated from the cantilever bending data of Krefft and Ernisse [26] as ~ 5 GPa, averaged over the implanted depth, which is assumed to be ~ 0.2 μm.*

---

*Unlike the $\{1 0 \bar{1} 2\}$ section used here, Eernisse's experiments used $[0 0 0 1]$, $[1 1 \bar{2} 0]$ and $[0 1 \bar{1} 0]$ sheet normal sections and this could affect the detailed compatability between his work and the present study.

Surface amorphization should result in a weaker layer which might be expected to deform and thus transfer the region of maximum compressive stress further below the surface. On thick samples, the surface layer has been observed to expand vertically [27] while the bending of thin specimens may result in strains which place the layer in tension and may lead to tearing as seen here. The further observation that amorphization of sapphire with Zr^+ also results in crazing, whereas amorphization with Ti^+ and Cr^+ does not [22], suggests that yielding of the amorphous material may be a sensitive function of its thickness, composition and damage state. This effect is being studied further.

The observations that lateral cracking is (a) less frequent, (b) less likely to break out and/or (c) transferred to further below the surface is compatible with a predominantly biaxial compressive surface stress state. The superposition of this stress upon the residual indentation stress field will be both to diminish the residual tensile stress near the surface and to transfer lateral crack opening to greater depths.

For radial cracking, the effect of the compressive stress appears to be to inhibit the attainment of the full semicircular crack configuration. Thus the cracks appear oblate to a greater or lesser degree (as shown in Fig. 10) with shorter traces on the surface. This is the principal reason why calculated K_{IC} values appear to increase after implantation. This increased K_{IC} value should not be regarded as an increase in bulk toughness but rather as reflecting the increased difficulty of a crack actually breaking through the surface. The K_{IC} calculation is further complicated by the change in hardness of the surface layer which alters the diagonal: crack trace ratio from which indentation toughness measurements are made, e.g. [12].

A number of workers have attempted to analyse the effect of a surface compressive layer on indentation/fracture behaviour but the cases considered (e.g. [28, 29]) have usually had a compressed layer of dimensions compatible with the indentation affected zone. The present case of a very thin ($\sim 0.2\,\mu$m) layer affecting the appearance of semicircular cracks of radius $\sim 20\,\mu$m is far less amenable to calculation. However, a crude lower-bound estimate of the compressive stress can be obtained by assuming that it is large enough to provide sufficient traction on the crack front element at the surface just to prevent crack growth. Such calculations yield values of the stress of the order of ≈ 0.2 GPa. A better calculation [30] based on the published indentation stress field of Yoffe [31], gives ≈ 0.1 GPa. These crude lower-bound estimates are not too dissimilar to the upper-bound estimate based on the data of Krefft and Eernisse [26]. Thus it seems that the near-surface compressive stresses can give rise to values of the order of 1 GPa for implantation into sapphire.

All the implantation stress controlled phenomena observed here, that is crazing, lateral crack suppression and changes in radial crack morphologies, are consistent with the presence of a predominantly biaxial compressive stress field close to the surface. There may be other components of the implantation-induced stress field (e.g. a compressive stress orthogonal to the surface) but we have no direct evidence for this from the present observations. The stress pattern is expected to vary with dose and specimen geometry and this is being explored further.

6.4. Plasticity and hardness

Surface softening has been clearly correlated with the presence of an amorphous layer, the degree of softening being dependent upon both the size of the amorphous layer and the scale of the test indentation. A previous paper [4] has established this behaviour for silicon and the present results confirm that sapphire behaves in a similar manner. Further, for sapphire, as for silicon, it would appear that once a certain "critical dose" is reached additional softening occurs as the amorphous layer rapidly (and unpredictably) thickens. For sapphire this dose is $\sim 3 \times 10^{17}\ Y^+\,cm^{-2}$ at 300 keV. This effect has many possible origins [4] including increased ion-transparency of the damaged layer and/or stress relief as the softened amorphous material yields and expands upwards in response to the compressive stresses (e.g. [27]) within it. However, for Y^+ in sapphire, implantation might be expected to increase the mean atomic number, and hence the ion stopping power of the implanted layer, thus rendering the layer increasingly ion-opaque. Stress relieving expansion may thus be the dominant effect controlling the unexpected thickening in this case. This thickening is accompanied by the first occurrence of crazing, thus adding credence to the premise that the yield stress of the layer decreases as the yttrium content increases. The hardness of the amorphous material has been estimated in two ways. Firstly, for specimen AY6, the depths of 25 gf Knoop indentations are ~ 0.3 μm and this is only slightly greater than the measured amorphous layer thickness of 0.23 μm. Thus the simplest estimate of the layer hardness is to take this Knoop hardness value as approximating to that of the amorphous material i.e. 2100 KHN (~ 2000 VHN). This method is probably an overestimate since it ignores both the fraction of the load supported by the substrate and the constraints on plasticity imposed by the substrate/layer interface [4]. A second estimate can be obtained by using the composite hardness model derived for this situation in our previous paper [4]. Taking the experimental hardness parameters of alumina as $H_{10\,\mu\mathrm{m}} = 3000 \pm 10\%$ and indentation size effect index (ISE index) = 1.64, and assuming that the amorphous layer probably has an ISE of ~ 2, then the hardness of the amorphous material is estimated to be between 500 and 1500 VHN (calculated for the extremes of the range of scatter of the observed low load/ISE parameter values).

The hardening observed for the lowest dose Y^+ implanted (AY1) sapphire specimen has been attributed to solid solution effects [22]. Certainly, Y^{3+}, being a large ion, should be capable of hindering dislocation motion as a result of the misfit strain field it introduces. However, we do not know the final charge state of the Y^+ implant in the highly damaged structure and any charge state other than 3+ might be expected to contribute further to the hardening by charge compensation effects (e.g. [32]). There may also be a substantial contribution from radiation hardening.

Finally, while the implantation-induced stresses have obvious effects upon fracture behaviour and promote crazing (Section 6.3), it may be that the stress field also has some effect upon plasticity and thus indentation hardness behaviour. For example, confining hydrostatic pressures of the order of the implantation-induced stresses reported have been reported to suppress massive fracture and promote plastic deformation (by slip and microfracture) in MgO [33]. Also, Haasen has suggested that, for dislocations in ionic crystals, hydrostatic compression might lower the Peierls stress by constricting dislocation cores and stacking faults [34]. However, such possibilities are only speculative at present, but may be clarified by further investigations.

7. Conclusions

This paper attempts to separate the various observed changes in near-surface mechanical properties of ion-implanted ceramics into two broad categories, namely, those influenced by the implantation-induced stresses (e.g. apparent K_{IC} values, indentation fracture morphologies) and those influenced by the presence of an amorphous layer (e.g. increased surface plasticity, decreased hardness). Preceding amorphization, there are also hardening effects probably associated either with solid solution effects of the implant species and/or with the radiation damage.

The dominant surface stress state produced by the implantation process is compressive and simple estimates suggest that it is of the order of 1 GPa. The observed stress related effects (i.e. crazing and changes in indentation fracture behaviour) are compatible with the stress state being principally biaxial compression in the plane of the surface. A major effect of the stress is to change the morphology of lateral fracture, both suppressing breakout in silicon and reducing the occurrence of this mode of indentation fracture in sapphire. While radial crack trajectories show no alteration on implantation, the extent of their traces on the surface is reduced so apparently increasing the K_{IC} values calculated from this fracture mode. Additionally, the surface stress state has been observed to produce surface crazing resulting from localized yielding of the softer amorphous material produced at high doses of Y^+ into sapphire.

As previously reported for silicon, high implantation doses ($\gtrsim 10^{17}$ ions cm^{-2}) have also been observed to result in a surface amorphous layer on sapphire. The production of this layer is well described by the simple quantitative model of Burnett and Page [4] and its genesis has been monitored by a range of microstructural techniques. The critical energy criterion for amorphizing sapphire has been estimated to be ~ 3×10^{23} keV cm^{-3} (~ 44 kJ mm^{-3}).

The hardness of the amorphous material has been estimated to be ~ 1000 VHN. Its occurrence results in surface softening as monitored by hardness tests where penetration depths are of the same order as the amorphous layer thickness. As previously reported for silicon [3, 4], a marked decrease in hardness was observed over the dose range when the amorphous layer thickness rapidly increases. The amorphous material appears sufficiently ductile to produce "pile-ups" of displaced material around hardness impressions. It also tears to produce crazes.

Hardening of sapphire was observed at doses of Y^+ lower than that required to produce amorphization and this is attributed to a possible mixture of solid solution and radiation hardening effects.

In conclusion, ion implantation has been observed to modify the detailed responses of both silicon and sapphire to indentation tests. The observed changes have been largely accounted for in terms of implantation-induced stresses, implantation-induced amorphization and, possibly, solid solution and radiation hardening effects.

Acknowledgements

The authors are indebted to Professor R. W. K. Honeycombe FRS for provision of laboratory facilities, Drs G. Dearnaley and N. Eyre for the provision of and technical assistance with both the implantations and the RBS analyses. PJB wishes to acknowledge SERC and AERE for the provision of a CASE award. We are also grateful to Mr P. J. C. Mathis (Texas Instruments (UK)) for the provision of the silicon specimens and GEC (Wembley) for the provision of the sapphire specimens. It is a pleasure to thank Dr E. H. Yoffe for invaluable discussions concerning the near-surface stress states.

Appendix

The distributions of both the implanted ions and resulting damage are often approximated to as Gaussian [7]; the Gaussian ion range profile being described by parameters R_p, the mean projected range, and ΔR_p, the standard deviation of R_p. The model due to Lindhard *et al.* [35, 36] has been used in this study to determine these parameters. Similarly, the damage distribution is described by $\langle X \rangle_D$, the mean depth at which displacement events occur (i.e. depth of maximum damage) and $\langle \Delta X_D \rangle$, the standard deviation of $\langle X_D \rangle$. Table III shows the range and damage parameters for the implant/substrate combinations studied here. The peak of the damage profile, at $\langle X_D \rangle$ below the surface, always lies above the peak of the concentration profile, R_p, and, for the ion species used in this study, the spread of the range profile is always greater than that of the damage profile. The exact relationship between the range and damage parameters is unclear, but the situation has been modelled by Winterbon *et al.* [37] as a function of M_2/M_1, the mean substrate atomic mass/ion mass.

TABLE III Range and damage parameters

Ion	Substrate	Energy (keV)	Range parameters (μm) (LSS)		Damage parameters (μm) (WSS)	
			R_p	ΔR_p	$\langle X_D \rangle$	$\langle \Delta X_D \rangle$
N^+	Silicon	45*	0.136	0.0472	0.110	0.0402
N^+	Silicon	90*	0.275	0.077	0.222	0.0656
Al^+	Silicon	300	0.0472	0.115	0.372	0.107
Y^+	Sapphire	300	0.080	0.0231	0.072	0.0383

*Components of the "Pimento" beam.

The ECP, RBS and TEM results of Section 3 (Table I) indicate that crystallinity is no longer detectable at doses of $\gtrsim 3 \times 10^{16}\ Y^+\ cm^{-2}$. In practice, there will be no discrete transition from crystalline to amorphous structures, rather a gradual transition from disordered, to highly disordered, to amorphous material as the dose is increased. However, it seems reasonable to use the dose given above as that above which the material is said to be amorphous. The dose may be converted to a damage level and this will correspond to a critical level of energy deposition. Hence we will refer to this as the critical energy criterion for amorphization (CECA).

For a given ion*, the total energy deposited by displacement events may be given by [7]

$$E_c(\text{keV}) \approx M_1\ (\text{a.m.u.}) \qquad \text{(A1)}$$

hence for a dose, ϕ, (conventionally expressed in ions cm^{-2}) the total energy deposited is

$$E_{\text{total}} \approx \phi M_1 \qquad \text{(A2)}$$

Hence, by combining Equation A2 with the form of the normalized Gaussian, the damage profile may be expressed in terms of energy deposition:

$$\text{Energy deposition (keV cm}^{-3}\text{)} \approx$$

$$\approx \frac{\phi M_1}{\langle \Delta X_D \rangle (2\pi)^{1/2}} \exp\left(\frac{-(X - \langle X_D \rangle)^2}{2 \langle \Delta X_D \rangle^2} \right) \qquad \text{(A3)}$$

---

*This assumes that the ion energy is initially greater than E_c, the displacement cut-off energy.

where X is the depth beneath the surface (in cm) with the damage parameters also expressed in cm. Clearly, amorphization will occur initially at the peak of the energy deposition profile (i.e. when $X = \langle X_D \rangle$) and hence, with a knowledge of the dose, ϕ_{crit}, at which amorphization first occurs, it is possible to use Equation 3 to determine the CECA for sapphire thus

$$\text{CECA (keV cm}^{-3}) \approx \frac{\phi_{\text{crit}} M_1}{\langle \Delta X_D \rangle (2\pi)^{1/2}} \quad \text{(A4)}$$

If ϕ_{crit} is taken as 3×10^{16} Y^+ cm^{-2}, then using the value of $\langle \Delta X_D \rangle$ derived from the Lindhard and Winterbon [35–37] models, Equation A4 yields a value of the CECA of 2.8×10^{23} keV cm^{-3}. This is approximately three orders of magnitude greater than that for silicon (previous estimates for the CECA of silicon range being from 5 to 10×10^{20} keV cm^{-3}) and reflects the greater atomic density of sapphire, the non-directional nature of its bonding [38] and the action of re-ordering processes occurring during implantation. If re-ordering did not occur then the calculated CECA would correspond to each atom being displaced ~ 50 times before amorphization occurred.

References

1. G. DEARNALEY, *Nucl. Inst. Methods* **189** (1980) 117.
2. *Idem*, *Trans. Inst. Met. Fin.* **56** (1978) 25.
3. S. G. ROBERTS and T. F. PAGE, in "Ion Implantation into Metals", edited by V. Ashworth, W. A. Grant and R. P. M. Proctoer (Pergamon, Oxford, 1982) p. 135.
4. P. J. BURNETT and T. F. PAGE, *J. Mater. Sci.* **19** (1984) 845.
5. J. R. MORRIS, *Nucl. Inst. Methods* **197** (1982) 147.
6. L. A. CRISTEL, J. F. GIBBONS and T. W. SIGMON, *J. Appl. Phys.* **52** (1981) 7143.
7. G. CARTER and W. A. GRANT, "Ion Implantation of Semiconductors", (Edward Arnold, London, 1976).
8. D. C. JOY, D. E. NEWBURY and D. L. DAVIDSON, *J. Appl. Phys.* **52** (1982) R81.
9. S. M. DAVIDSON and G. R. BOOKER, *Radiat. Eff.* **6** (1970) 33.
10. B. R. LAWN and D. B. MARSHALL, *J. Amer. Ceram. Soc.* **62** (1979) 347.
11. B. R. LAWN and A. G. EVANS, *J. Mater. Sci.* **12** (1977) 2195.
12. A. G. EVANS, *Amer. Soc. Test Mater. Spec.* (1979) Technical Publication no. 678.
13. B. R. LAWN, A. G. EVANS and D. B. MARSHALL, *J. Amer. Ceram. Soc.* **63** (1980) 574.
14. B. R. LAWN and T. R. WILSHAW, *J. Mater. Sci.* **10** (1975) 1049.
15. K E. PUTTICK and M. M. HOSSEINI, *J. Phys. D: Appl. Phys.* **13** (1980) 875.
16. G. R. ANSTIS, P. CHANTIKUL, B. R. LAWN and D. B. MARSHALL, *J. Amer. Ceram. Soc.* **64** (1981) 533.
17. D. B. MARSHALL and A. G. EVANS, *ibid.* **64** (1981) C182.
18. D. B. MARSHALL, B. R. LAWN and A. G. EVANS, *ibid.* **65** (1982) 561.
19. M. G. S. NAYLOR and T. F. PAGE, *J. Microsc.* **130** (1983) 345.
20. R. W. ARMSTRONG and C. Cm WU, *J. Amer. Ceram. Soc.* **61** (1978) 102.
21. G. R. SAWYER, P. M. SARGENT and T. F. PAGE, *J. Mater. Sci.* **15** (1980) 1001.
22. P. J. BURNETT and T. F. PAGE, Proceedings of the Conference on Plastic Deformation of Ceramic Materials, Penn State University, 1983, edited by R. C. Bradt and R. E. Tressler, (Plenum Press, New York, in press).
23. *Idem*, to be published.
24. S. G. ROBERTS, (1982) PhD thesis, University of Cambridge.
25. C. J. McHARGUE, H. NARAMOTO, B. R. APPLETON, C. W. WHITE and J. M. WILLIAMS, *Proc. Mat. Res. Soc.* **7** (1982) 147.
26. G. B. KREFFT and E. P. EERNISSE, *J. Appl. Phys.* **49** (1978) 2725.
27. C. J. McHARGUE and J. M. WILLIAMS, *Proc. Mat. Res. Soc.* **7** (1982) 303.
28. D. B. MARSHALL, B. R. LAWN and P. CHANTIKUL, *J. Mater. Sci.* **14** (1979) 2225.
29. P. CHANTIKUL, D. B. MARSHALL, B. R. LAWN and M. G. DREXHAGE, *J. Amer. Ceram. Soc.* **62** (1979) 551.
30. E. H. YOFFE, private communication (1983).
31. *Idem*, *Phil. Mag.* **A46** (1982) 617.
32. T. E. MITCHELL and A. H . HEUER, *Mat. Sci. Eng.* **28** (1977) 81.
33. M. S. PATTERSON and K. W. WEAVER, *J. Amer. Ceram. Soc.* **53** (1970) 463.
34. P. HAASEN, *J. Physique Coll.* **C7** (1974) 167.
35. J. LINDHARD, M. SCHARFF and H. E. SCHIØTT, *Matt. Fys. Med. Kgl. Dansk. Vid. Selsk.* **33** (1963) No. 14.
36. B. J. SMITH, in "Ion Implantation", edited by G. Dearnaley, J. H. Freeman, R. S. Nelson and J. Stephen, (North-Holland, Amsterdam, 1973).
37. K. B. WINTERBON, P. SIGMUND and J. B. SANDERS, *Matt. Fys. Med. Kgl. Dansk. Vid. Selsk.* **37** (1970) No. 14.
38. A. ALI, W. A. GRANT and P. J. GRUNDY, *Phil. Mag.* **37** (1978) 353.

Received 2 December
and accepted 21 December 1983